ChemComm

Polarized Light Through Polycrystalline Vaterite Helicoids

Journal:	*ChemComm*
Manuscript ID	CC-COM-03-2020-001958.R1
Article Type:	Communication

COMMUNICATION

Polarized Light Through Polycrystalline Vaterite Helicoids

Melissa Tan,[a] Wenge Jiang[b]*, Alexander T. Martin,[a] Alexander G. Shtukenberg,[a] Marc D. McKee,[cd]* Bart Kahr[a]*

Received 00th XXXX 2020,
Accepted 00th XXXX 2020

DOI: 10.1039/x0xx00000x

Abstract. Vaterite helicoids [Jiang, W. *et al*. *Nature Communications,* 2017, 8, 15066]. are chiral, polycrystalline suprastructures grown in the presence of the amino acids, aspartic (Asp) or glutamic (Glu) acid, that are abundant in proteins regulating biomineralization. These complex objects are composed of hexagonal vaterite nanocrystals assembled as curved-edge platelets that form chiral ensembles. The sense stacked platelets is correlated with the stereochemistry of the amino acid additive: *L*-Asp gives counterclockwise architectures while *D*-Asp gives the clockwise enantiomorphs. As new layers stack, platelets become progressively inclined with respect to the substrate suface. The growth and structure of vaterite helicoids was originally evidenced by electron microscopy and atomic force microscopy Here, we develop an optical model for describing polarized light transmission through helicoids as measured by Mueller matrix polarimetry. The close agreement between experimental measurements and simulation confirms that the propellor-like organization of inclined platelets creates optically active structures determined by growth additive stereochemistry. The microscopy employed demonstrates the information that can be obtained by complete polarimetry using a camera as a light detector, and they could well be applied profitably to all manner of complex structures organized from anisotropic particles.

Vaterite helicoids – polycrystalline ensembles of a phase of $CaCO_3$ grown in the presence of chiral additives – were recently characterized in great detail by electron microscopy, atomic force microscopy and X-ray microanalysis.[1,2] While polarized light microscopy has long been a standard technique for characterizing single crystals and mineral grains, our interest has been focused on the study of polarized light transmission in polycrystalline materials.[3-10] Here, an inverted light microscope, customized with polarization state modulators based on dual rotating wave plates,[11,12] is used to simultaneously map the linear and circular anisotropies in chiral helicoids of vaterite (Figure 1). This so-called Mueller matrix microscopy, named for the recovery of the Mueller or polarization transformation matrix, can provide unique structural information in complex, organized systems constructed from misaligned optically anisotropic components. Such a characteristics can be found not only in the vaterite helicoids studied herein, but in biominerals and biomineral-like materials,[13] with hierarchical structures in addition to the polycrystalline spherulites just cited.[3-10]

The microscope design is described in detail elsewhere.[14,15] In short, continuous rotation of a pair of quarter-wave plates, with respect to stationary linear polarizers, generates a smoothly varying, time-dependent intensity signals at the detector that is subsequently demodulated to recover the Mueller matrix, **M**, a sixteen-element transformation matrix that relates the polarization state of an incident beam of light, expressed as a four-element Stokes vector **S**, to its corresponding output vector: $\mathbf{S}_{out} = \mathbf{M}\mathbf{S}_{in}$. Data are displayed as a 4×4 array of images each representing the spatial variance of one of the elements of the matrix (normalized by M_{11}). The microscope was built from a commercial inverted microscope (Zeiss ZM1) to which the mechanical modulators, built from 3D-printed and laser-cut parts, were added, an implementation that can be imitated at modest expense.[15]

The elements of **M** are real-valued, measurable, and completely describe the polarization-dependent linear optical effects. In general, each element of **M** represents a convolution of contributions from several optical constants; consequently, linear and circular anisotropies cannot be interpreted from **M** directly but must be recovered through matrix decomposition methods such as the differential analysis.[16] The polarization state of light propagating in a non-depolarizing medium can be described by a first-order differential equation: $d\boldsymbol{S}/dz = m\boldsymbol{S}$, where m is the differential Mueller matrix that transforms the Stokes vector over an infinitely small pathlength, z. Integrating the differential equation yields: $\boldsymbol{S}_{out} = e^{mz}\boldsymbol{S}_{in} = \mathbf{M}\boldsymbol{S}_{in}$. The matrix logarithm of **M**, which we define as **L**, provides a numerical approximation to m that deconvolves linear and circular anisotropies, revealing each optical effect as a unique element in the 4×4 matrix where

[a] Department of Chemistry and Molecular Design Institute, New York University, New York City, NY, 10003, USA. Email: bart.kahr@nyu.edu
[b] Department of Chemistry, Tianjin Key Laboratory of Molecular Optoelectronic Sciences, and Tianjin Collaborative Innovation Center of Chemical Science & Engineering, Tianjin University, Tianjin, PR China, 300072 Email: wengejiang_tju@163.com
[c] Faculty of Dentistry, McGill University, Montreal, Quebec, Canada H3A 0C7
[d] Department of Anatomy and Cell Biology, Faculty of Medicine, McGill University, Montreal, Quebec, Canada H3A 0C7. Email: marc.mckee@mcgill.ca

$$\mathbf{L} = \begin{bmatrix} -\mathrm{A} & -\mathrm{LE} & -\mathrm{LE}' & \mathrm{CE} \\ \mathrm{LE} & -\mathrm{A} & \mathrm{CR} & \mathrm{LR}' \\ \mathrm{LE}' & -\mathrm{CR} & -\mathrm{A} & -\mathrm{LR} \\ \mathrm{CE} & -\mathrm{LR}' & \mathrm{LR} & -\mathrm{A} \end{bmatrix} \approx \begin{bmatrix} m_{11} & m_{12} & m_{13} & m_{14} \\ m_{21} & m_{22} & m_{23} & m_{24} \\ m_{31} & m_{32} & m_{33} & m_{34} \\ m_{41} & m_{42} & m_{43} & m_{44} \end{bmatrix}.$$

Here LE and LE' refer to differential extinction of linearly polarized light along the 0° and 90° azimuthal directions and along the −45° and 45° directions, respectively, while LR and LR' describe linear retardance for the same polarization states. Elements along the anti-diagonal represent circular effects, circular retardance (CR) and circular extinction (CE), while diagonal elements represent the isotropic absorption, *A*.

Vaterite helicoids, grown by adding chiral acidic amino acids, undergo morphological changes during growth.[1,2] Initially, inclined platelets crystallize near the perimeter of a disc-shaped substrate of vaterite. The subsequent addition of platelets yields a dimple at the core of the disc, a characteristic feature of young helicoids (Figure 1a,d). Platelets converge at the centre of the disc during the intermediate growth stage (Figure 1b,e). Mature helicoids become crowded, forcing new platelets to progressive incline until they reach a vertical orientation (Figure 1c,f).[2] Representative measurements between glass coverslips in oil (Zeiss Immersol 518F, RI = 1.518) of young, intermediate, and mature helicoids obtained at normal incidence in orthoscopic 500 nm transmission are displayed in Figure 1g-i, alongside their corresponding differential Mueller matrices in Figure j-l. The optical complexity increases with growth.

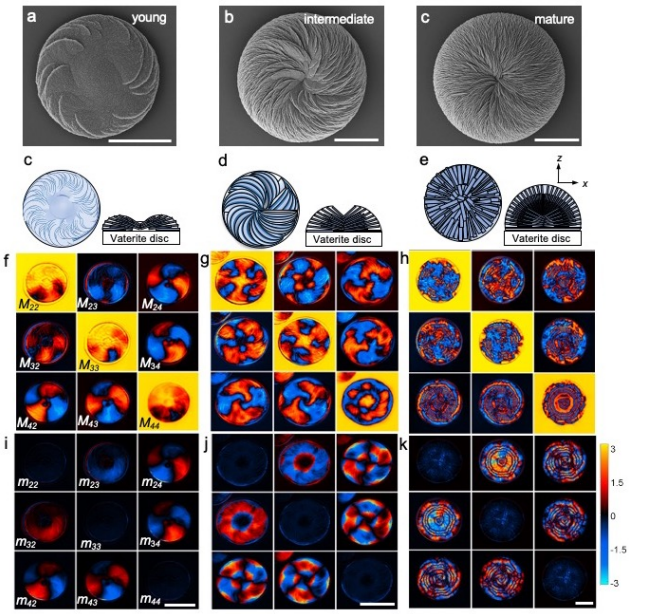

Figure 1. (a-c) Scanning electron micrographs of platelet arrangements in vaterite helicoids in young (a), adolescent (b) and mature (c) growth stages with *L*-Asp and accompanied by a schematic diagrams (d-f) illustrating young (d), adolescent (e), and mature (f) vaterite helicoid morphologies from above, as in the SEMs, and from the sides. *D*-Asp gives enantiomorphs not shown. See refs. 1 and 2. SEM scale bars are 25 μm. Normalized (left, scale = -1 +1) and differential (right, scale = rad) Mueller matrix images of young (g and j), adolescent (h and k), and mature (i and l) vaterite helicoids measured in orthoscopic transmission illumination at λ = 500 nm. Only the nine elements in the lower right are shown. The near zero intensity calculated in the first row and column of the differential Mueller matrix (not shown for clarity) indicates that as expected, that polycrystalline architectures of vaterite do not exhibit differential absorption at λ = 500 nm. In contrast, the last row and column exhibit complicated patterns attributed to the differential retardance of light polarized along the *x* and *y*-axes (LR), and along +/-45 deg (LR'). This LR arises from the inclination and misorientation of platelets, generating a misalignment of the refractive index ellipsoid in adjacent platelet layers. Ultimately, the concerted fanning of platelets produces circular retardance (CR), as determined in m_{23} and m_{32} of the differential Mueller matrix. Matrix scale bars are equal to 50 μm.

As expected from the definition of **L**, the matrix elements along the antidiagonal, m_{23} and m_{32}, are oppositely signed. The largest values of LR and LR', determined by m_{24}, m_{34}, m_{42}, and m_{43}, map to areas where daughter platelets have grown atop underlying layers. The gradual inclination and misalignment of platelets along *z* creates a dissymmetry between anisotropic substructures. The emergence of CR, determined from m_{23} and m_{32}, arises from the spiralling organization of the vaterite platelets in non-normal incidence. The CR initially grows as the helicoid develops (Figure 1i and 1k) but becomes difficult to parse as the number of misoriented and inclined anisotropic platelets increases (Figure 1j).

Linear and circular effects are displayed in Figure 2. The CR is defined as the average of the difference between m_{23} and m_{32}, whereas the $|\mathrm{LR}| = ((\mathrm{LR})^2 + (\mathrm{LR}')^2)^{1/2}$. The magnitude of the linear retardance is similar for helicoids of the same size, irrespective of their chirality. In contrast, the CR of helicoids grown with *L*-Asp and *D*-Asp are oppositely signed: counter-clockwise/CCW (clockwise/CW) structures give positive (negative) CR, respectively (Figure 2). Although individual platelets are uniaxial, the suprastructure is not. Near the centre, LR and LR' are zero because insufficient time has elapsed for platelets to grow in non-normal orientations. Thus, near the core, light travels along the high symmetry axis of an approximately uniaxial system. The CR likewise disappears at the centre as it arises not from natural optical activity but rather from the sense of twist relating stacked anisotropic lamellae.

The spiralling, inclined platelets are analogous to the edge-on to flat-on evolution of twisting crystalline ribbons in banded spherulites.[10] Spherulite growth is often quite regular, enabling light propagation to be described by two parameters, ω and Φ (Figure 3). ω defines the twist angle as a function of the radial distance, *R*, from the spherulite centre, while Φ describes the maximum offset, the angle between the radial vectors of the first and P^{th} lamellae, where *P* is the total number of layers along *z*. The average offset angle, φ_p, between any layer (p = 1,… *P*) and *P*-1 depends on both Φ and on the radial coordinate.[10]

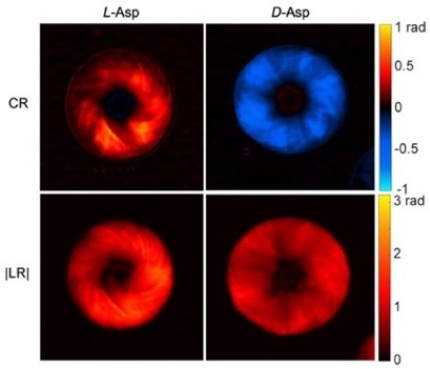

Figure 2. Optical properties derived from **L** for measurements obtained in orthoscopic transmission illumination at λ = 550 nm of young, chiral vaterite helicoids grown in the

presence of *L*-Asp or *D*-Asp. While the magnitude of the LR is similar, the CR of helicoids grown from *L*- or *D*-Asp are oppositely signed. The bottom edge of each image is 50 μm.

Although vaterite platelets do not twist about the radial direction of the vaterite disc, these sub-units do become inclined with respect to the surface of the substrate and in relation to each other to accommodate the addition of layers along +*z*. Consequently, the exposed platelet face evolves over time from flat-on to edge-on. This inclination is simultaneously accompanied by spiralling in the *xy* plane, creating a misorientation between neighbouring sub-units. These structural attributes can be modelled by the previously described geometric parameters ω and Φ.

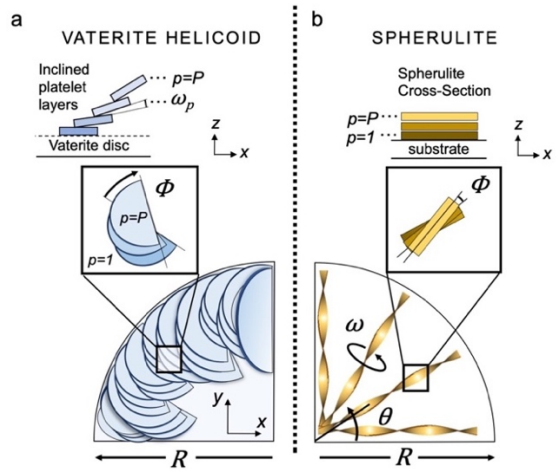

Figure 3. Illustration of the mesoscale structure of one-quarter of a chiral, vaterite helicoid (a) and a spherulite composed of twisting ribbons (b). Vaterite helicoids grow as platelets that initially nucleate on a substrate disc of vaterite. The presence of *L*-Asp or *D*-Asp achieves a CCW or CW organization, respectively. In helicoids, the maximum offset angle, Φ, in the *xy* plane for a stack of *P* platelets is defined by the angle between the initial plate, $p = 1$, and uppermost plate, $p = P$. This is illustrated in detail in the enlarged panel. A view of platelets in cross-section is drawn above the inset and describes the gradual inclination of platelets along *z*. The mesoscale structure of spherulites is analogous to vaterite helicoids. Each twisted ribbon in (b) represents a bundle of lamellae that rotate around the length of the stack. The orientation of individual lamellae within the ensemble is related by φ. A cross-sectional view of a spherulite shows the difference between vaterite helicoids and spherulites. Whereas vaterite platelets twist out of the *xy* plane, spherulite lamellae precess around the radial growth direction, *R*.

In helicoids, the magnitude of the overall offset angle increases with *z* where *z*=0 represents the base of the once amorphous disc. Modelling the offset angle requires knowing how layers are enumerated with respect to φ_p. $\left(\frac{p-1}{P-1}\right)$ defines the average offset angle as the angle between the radial vectors of the p^{th} layer and the initial plate, $p = 1$. In general, helicoids are thinner at their centre. Thickness increases along the radial direction from the disc, tapering near the edge of the structure. This line shape is modelled by $\sin(t)$, where $t = \frac{r}{R}(a\pi)$. The variable *a* alters how the thickness evolves as the radial position, *r*, approaches *R*, the helicoid radius. Thus, the average offset angle can be represented as

$$\varphi_p = \sin(t)\Phi\left(\frac{p-1}{P-1}\right).$$

The normalized Mueller matrix was simulated as an ensemble of vaterite platelets in Cartesian space. The *x*-axis is coincident with the radial direction of the vaterite disc while the *z*-axis is projected out of the plane of the page (Figure 4). The electric permittivity tensor of the p^{th} plate at an angle ϑ from the *x*-axis is defined by

$$\boldsymbol{\varepsilon}_p = \mathbf{R}_p \begin{bmatrix} {n_x}^2 & 0 & 0 \\ 0 & {n_x}^2 & 0 \\ 0 & 0 & {n_z}^2 \end{bmatrix} \mathbf{R}_p,$$

where n_x and n_z refer to the refractive indices of vaterite, determined previously as $n_x = 1.55$ and $n_z = 1.65$.[17] The matrix $\mathbf{R}_p$ is defined as a product of rotation matrices:

$$\mathbf{R}_p = \mathbf{R}_z(\theta + \varphi_p)\,\mathbf{R}_x(\omega_p t).$$

The Mueller matrix of each plate, $\mathbf{M}_p$, is determined by evaluating the matrix exponential of a sparsely populated differential Mueller matrix,

$$\mathbf{M}_p = \exp\begin{bmatrix} 0 & 0 & 0 & 0 \\ 0 & 0 & 0 & \mathrm{LB}' \\ 0 & 0 & 0 & -\mathrm{LB} \\ 0 & -\mathrm{LB}' & \mathrm{LB} & 0 \end{bmatrix}.$$

Bulk propagation simulated by multiplying each layer matrix: $\mathbf{M}_p{}^{P-1}$. The product is subjected to a rotation about the azimuth, ϑ, in order to construct the Mueller matrix of a helicoid.

We relied upon the structural model elucidated by SEM to establish values for *P*, ω, φ, and helicoid thickness *d*.[1,2] Every platelet is approximately inclined by $\omega_p = 6°$ from the platelet beneath (Figure 4). The 15$^{\text{th}}$ platelet thereby represents the first vertical layer in the structure. From this point onwards during growth, as new platelets continue to form to enlarge the suprastructure, daughter layers are rotated with respect to mother layers by $\pm$ 22.5° about the *z*-axis. This provides an approximate value for the maximum offset angle, Φ. Ultimately, although vaterite helicoids are consistently quite regular, many helicoids do not display perfect azimuthal symmetry. Differences in mesoscale structure are easily explained by local variations in the growth environment or by the stochastic nature of low-angle branching; our model can only describe the average radial structure of the ensemble.

The normalized Mueller matrix, **M**, of a young helicoid (Figure 1g) measured at 500 nm in normal incidence is modelled in Figure 4. The platelets have nearly converged at the centre of the vaterite disc; thus, we approximate the number of layers as $P = 8$. In theory, if every platelet is inclined by $\omega_p = 6°$, then the maximum inclination angle, ω, defined as the angle between the substrate disc and *P*, should be 48°. In our model, the best fit was obtained using $\Phi = 33.15°$, $\omega = 54°$, $[n_x, n_y, n_z] = [1.55, 1.55, 1.65]$, and $d = 750$ nm. The difference between the expected value of ω and the simulation parameter suggests that *P* may differ around the helicoid, or that there may be some variation in the inclination ω_p. |LR| of an ensemble of CCW and CW structures (Figure 2) can vary around the azimuth of helicoids. The agreement between the model and the measurements in Figure 4 suggests that the optical properties assayed can be simulated by describing the relationship between vaterite platelets in the *xy* plane and modelling their inclination along *z*.

In general, varying thickness of individual platelets, *d*, affects the simulated intensity. Increasing the offset angle (Φ)

or the inclination angle (ω), prompts an evolution of the patterns determined by the simulation (Movie S1 showing variance of the simulation as a function of Φ); the "pinwheels" are oriented in the direction of their twist. Further structural analysis via SEM and high-resolution XRD during various stages of growth may be required to develop a more comprehensive view of the variability of helicoid mesoscale structure to further inform the optical model and analysis. Using the method presented here, the chirality of the intensity plots is well determined from the sign of Φ. This is consistent with our expectations since Φ affects whether the simulated stack of platelets is rotated around *z* in a CW or CCW direction.

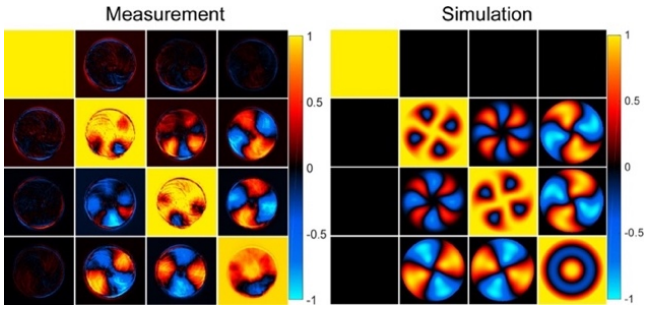

Figure 4. Simulation of the measured Mueller matrix, **M**, of a young helicoid obtained at λ = 500 nm in normal incidence transmission using P = 8, Φ = 33.15°, ω = 54°, [n_x, n_y, n_z] = [1.55, 1.55, 1.65], and d = 750 nm. Values are normalized to M_{11} and are unitless.

Polarimetric experiments confirm that helicoids of opposite sense generate oppositely signed CR. Light propagating through CCW (CW) structures yields positive (negative) CR (Figure 3). The circular anisotropy arises from the mesoscale organization of vaterite platelets. Optical activity of this kind was first described for a stack of misaligned mica plates.[18] More recently, spherulites of polylactide produced CR when tilted with respect to the wave vector.[7] The sign of this signal was coupled to the sign of the tilt as for vaterite here. Optical models show how LR ultimately becomes manifest as CR through the concerted spiralling arrangement of platelets, corroborating the features of the structural model previously proposed.[1,2]

The optical analysis illustrated herein is applicable to a wide variety of organized structures with similar features, including, but by no means limited to the following: coccolithoxphores,[19] foraminifera skeletons,[20,21] sheaves of fluorine substituted hydroxy apatite,[22] and potassium dichromate thin films.[23] In this work we demonstrated that just as the dissymmetric arrangements of polarized atoms and groups of atoms in molecules in solution can give rise to a sense dependent optical activity, the dissymmetric arrangement of anisotropic optical elements at the mesoscale as can be detected by complete polarimetry. We expect this approach may be widely used, and applicable and informative, in the biomineralization field.

Conflicts of interest

There are no conflicts to declare.

Acknowledgements

This work was primarily supported by the NIH (5R21GM107774-02). MT and AGS received partial support from the NYU MRSEC Program of the NSF under awards DMR-0820341 and 1420073. MT also received support through the Margaret and Herman Sokol Fellowship from the NYU Department of Chemistry. MDM received funding from the NSERC of Canada (RGPIN-2016-05031) and the Canada Research Chairs program. MDM is a member of the FRQ-S Network for Oral and Bone Health Research. WJ received support from the National NSF of China (21975179). The contributions of Dr. S. Nichols to the microscope implementation cannot be overstated.[15]

Notes and references

1 W. Jiang, M. S. Pacella, D. Athanasiadou, V. Nelea, H. Vali, R. M. Hazen, J. J. Gray and M. D. McKee, *Nature Commun*., 2017, **8**, 15066.
2 W. Jiang, M. S. Pacella, H. Vali, J. J. Gray and M. D. McKee, *Sci. Adv*., 2018, **4**, eaas9819.
3 W. Jiang, X. Yi and M. D. McKee, *Mater. Horiz*. 2019,**6**, 1974-1990.
4 E. Gunn, R. Sours, J. B. Benedict, W. Kaminsky and B. Kahr, *J. Am. Chem. Soc*., 2006, **128**, 14234-14235.
5 B. Kahr and J. H. Freudenthal, *Chirality,* 2008, **20**, 973-977.
6 J. H. Freudenthal, E. Hollis and B. Kahr, *Chirality*, 2009, **21**, E20-E27.
7 H.-M. Ye, J. Xu, J. H. Freudenthal and B. Kahr, *J. Am. Chem. Soc*., 2011**, 133**, 13848-13851.
8 X. Cui, A. L. Rohl, A. G. Shtukenberg and B. Kahr, *J. Am. Chem. Soc*., 2013, **135**, 3395-3398.
9 X. Cui, A. G. Shtukenberg, J. H. Freudenthal, S. M. Nichols and B. Kahr, *J. Am. Chem. Soc*., 2014, **136**, 5481-5490.
10 X. Cui, S. M. Nichols, O. Arteaga, J. H. Freudenthal, F. Paula, A. G. Shtukenberg and B. Kahr, *J. Am. Chem. Soc*., 2016, **138**, 12211-12218.
11 L. Helmbrecht, M. Tan, R. Röhrich, B. Ortiz Kessels, F. Koenderink, B. Kahr and W. L. Noorduin *Adv. Funct. Mater.*, 2020, doi.org/10.1002/adfm.201908218.
12 R. M. A. Azzam, *Opt. Lett*. 1978, **2**, 148–150.
13 D. H. Goldstein, *Appl. Opt*. 1992, **31**, 6676–6683.
14 O. Arteaga, M. Baldrís, J. Antó, A. Canillas, E. Pascual and E. Bertran, *Appl. Opt.*, 2014, **53**, 2236-2245.
15 S. M. Nichols, PhD Dissertation, New York University, 2018.
16 R. M. A. Azzam, *J. Opt. Soc. Am.*, 1978, **68**, 1756-1767.
17 J. Johnston, H. E. Merwin and E. D. Williamson, E. D. *Am. J. Sci.*, 1916, **4**, 473-512.
18 E. Reusch, *Ann. Phys.* 1869**, 214**, 628.
19 J. R. Young and K. Henriksen, *Rev. Mineral. Geochem*., 2003, **54**, 189–215.
20 M. D. Georgescu, *J. Micropaleontol*., 2010, **29**, 149–161.
21 N. O. Eguchi, H. UjiieÅL, H. Kawahata and A. Taira, *Mar. Micropaleontol*., 2003, **48**, 149–163.
22 Y. J. Wu, T. W. T. Tsai and J. C. C. Chan, *Cryst. Growth Des*., 2012, **12**, 547–549.
23 Y. Oaki and H. Imai, *J. Am. Chem. Soc*., 2004, **126**, 9271–9275.

Footnote

†Electronic supplementary information (ESI) available. Movie S1. See DOI: X.aaa

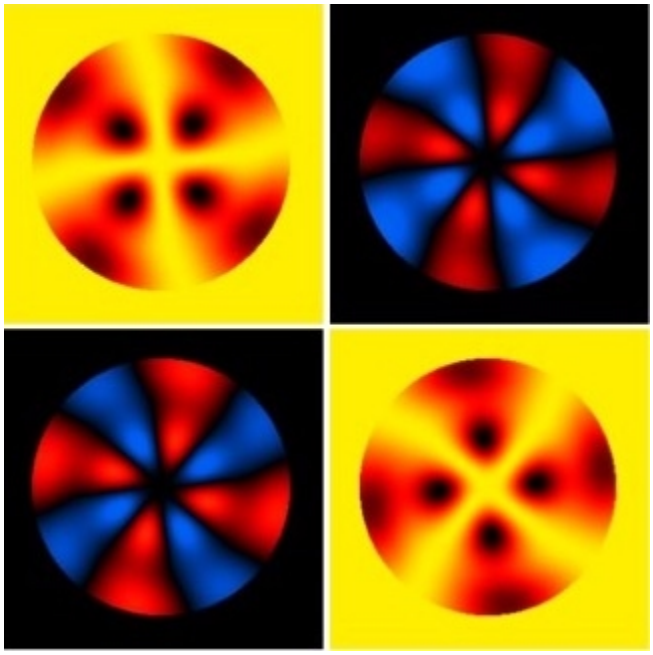

75x75mm (108 x 108 DPI)